ADVANCED FUNCTIONAL MATERIALS
www.afm-journal.de

Environmental Control of Triplet Emission in Donor–Bridge–Acceptor Organometallics

*Jiale Feng, Lupeng Yang, Alexander S. Romanov, Jirawit Ratanapreechachai, Antti-Pekka M. Reponen, Saul T. E. Jones, Mikko Linnolahti, Timothy J. H. Hele, Anna Köhler, Heinz Bässler, Manfred Bochmann, and Dan Credgington**

Carbene-metal-amides (CMAs) are a promising family of donor–bridge–acceptor molecular charge-transfer (CT) emitters for organic light-emitting diodes. A universal approach is demonstrated to tune the energy of their CT emission. A blueshift of up to 210 meV is achievable in solid state via dilution in a polar host matrix. The origin of this shift has two components: constraint of thermally-activated triplet diffusion, and electrostatic interactions between guest and polar host. This allows the emission of mid-green CMA archetypes to be tuned to sky blue without chemical modifications. Monte-Carlo simulations based on a Marcus-type transfer integral successfully reproduce the concentration- and temperature-dependent triplet diffusion process, revealing a substantial shift in the ensemble density of states in polar hosts. In gold-bridged CMAs, this shift does not lead to a significant change in luminescence lifetime, thermal activation energy, reorganization energy, or intersystem crossing rate. These discoveries offer new insight into coupling between the singlet and triplet manifolds in CMA materials, revealing a dominant interaction between states of CT character. The same approach is employed using materials which have been chemically modified to alter the energy of their CT state directly, shifting the emission of sky-blue chromophores into the practical blue range.

1. Introduction

Thin-film organic light-emitting diodes (OLEDs) have developed into a flourishing commercial industry in the last few decades. In 1987, Tang and Van Slyke demonstrated first "sandwich structure" OLED utilizing fluorescent emission from spin-singlet states.[1] Second-generation phosphorescent OLEDs utilizing emission from spin-triplet states, developed a decade later, exhibit high efficiency and significant synthetic tuneability, making them the current best candidates for lighting and display technologies.[2] However, efficient deep blue OLEDs remain one of the key challenges limiting their broader application, due to low quantum efficiency and short operational lifetime.[3] Within this sphere, a new class of donor–bridge–acceptor carbene-metal-amide (CMA) emitters has been developed that exhibit high electroluminescence quantum efficiency at high brightness and rapid (sub-microsecond) harvesting of triplet states.[4] Short emission lifetime is critical for preventing bimolecular exciton annihilation reactions, which are implicated in efficiency roll-off and reduced operational stability.[5,6] CMA emitters exhibit flexible molecular design with low synthetic complexity[7–11] and benign solid state interactions.[12] Their combination of low-exchange energy and high spin–orbit coupling occupies a space between traditional phosphorescent emitters and more recently developed thermally activated delayed fluorescence (TADF) compounds, leading to significant interest in their underlying emission mechanism.[13–15]

The archetype of the family, CMA1, is a mid-green emitter both in solution and in amorphous thin film. However, unlike many other triplet-harvesting organic and organometallic archetypes, CMA materials exhibit three features which allow additional routes to tune emission characteristics: 1) significant geometric flexibility, allowing tuning of excited state energies through control of geometry, 2) large negative absorption solvatochromism due to a significant electrostatic dipole in the ground state, and 3) lack of concentration quenching, allowing flexibility in host:dopant ratio and host choice.

J. Feng, L. Yang, J. Ratanapreechachai, S. T. E. Jones, A.-P. M. Reponen, Dr. T. J. H. Hele, Dr. D. Credgington
Cavendish Laboratory
Department of Physics
University of Cambridge
JJ Thomson Avenue, Cambridge CB3 0HE, UK
E-mail: djnc3@cam.ac.uk
Dr. A. S. Romanov, Prof. M. Bochmann
School of Chemistry
University of East Anglia
Earlham Road, Norwich NR4 7TJ, UK
Prof. M. Linnolahti
Department of Chemistry
University of Eastern Finland
Joensuu Campus, FI-80101 Joensuu, Finland
Prof. A. Köhler, Prof. H. Bässler
Experimental Physics II and Bayreuth Institute of Macromolecular Science (BIMF)
Department of Physics
University of Bayreuth
Bayreuth 95440, Germany
The ORCID identification number(s) for the author(s) of this article can be found under https://doi.org/10.1002/adfm.201908715.

DOI: 10.1002/adfm.201908715

Here, we show how the emission of CMA1 can be tuned by utilizing intermolecular interactions with a variety of host materials to both restrict triplet diffusion and shift the density of excited states. The result is that the photoluminescence peak of CMA1 can be increased in energy by 210 meV, into the blue color range, without altering its chemical structure. We determine that static electrostatic interactions are one of the most important parameters for these composites, whereas for organic TADF-type emitters, the influence of the host is typically to redshift the emission through dynamic polarizability.[16–19] Despite the significant change in emission energy achieved, we find that the low activation energy for delayed emission and short room-temperature emission lifetimes are preserved. We use these new experimental findings to test current quantum-chemical descriptions of CMA emission, and provide a better understanding of its mechanism. We go on to show that this approach extends to other gold CMA complexes across the visible spectrum, allowing the emission energy for each to be tuned over a 150–200 meV range.

2. Results and Discussion

2.1. The CMA1 Molecule

The chemical structure of CMA1 is illustrated in **Figure 1**a. In the ground state S_0, the CAAC group is relatively electron deficient, while the amide is electron rich, creating a ground-state electrostatic dipole moment of order 15 D aligned along the C-Au-N axis, hereafter taken as the *z*-axis of the molecule.[14] This large ground-state dipole is unusual for organic donor–acceptor-type emitters, with important implications for the manipulation of emission energy (vide infra). The highest occupied molecular orbital (HOMO) and lowest unoccupied molecular orbital (LUMO) of CMA1, calculated by density functional theory (DFT) utilizing the hybrid MN15 functional with the def2-TZVP basis set are presented in Figure 1b. The HOMO resides primarily on the amide, the LUMO on the carbene. Of order 3.0/11.4% of the electron density in the HOMO/LUMO resides on the metal, with largest contributions from the $5d_{yz}/5p_y$ atomic orbitals, respectively, where the carbazole is taken to lie in the *x*-*z* plane. Excitation from S_0 to S_1 is dominated by a HOMO–LUMO transition (natural transition orbitals comprise 98% HOMO–LUMO), which spans the metal bridge and has significant charge-transfer (CT) character, shifting electron density back from the amide to the carbene group. This reduces the electrostatic dipole to ≈5 D and reverses its sign.[4,20]

In addition to direct absorption to the singlet CT state, optical absorption spectra of CMA1 show features related to ligand-centered excitations of the carbene and amide groups (Figure S1, Supporting Information). For CMA1, the photoexcited CT singlet crosses to the triplet manifold within around 5 ps, with subsequent unstructured emission on sub-microsecond time scales.[4] The steady-state emission peak is around 520 nm (green region) in neat film at 300 K, see **Figure 2**a, with a Stokes' shift of 795 meV (measured peak-to-peak). The large Stokes' shift has been assigned in previous reports to a combination of fast vibrational relaxation followed by torsional relaxation from a coplanar to a twisted geometry, which narrows the S_1–S_0 energy gap.[20]

In solution, the CT band of CMA1 exhibits large negative absorption solvatochromism, consistent with the ordering of polar solvents around the large ground-state dipole, stabilizing S_0 and destabilizing S_1.[14] Emission shows weak positive solvatochromism, consistent with much weaker ordering of solvent around the smaller S_1 dipole, see Figures S2 and S3 in the Supporting Information. In neat thin film, the CT absorption band is broader and peaks at 388 nm, between the values of toluene (407 nm) and dichloromethane (385 nm) solutions.

2.2. Dopant Concentration and Role of Diffusion for CMA1 in PVK Host

We first examine the effect of host on emission energy in the absence of significant electrostatic interactions. Poly(9-vinylcarbazole) (PVK) is a common polymer host material for solution processed OLEDs, possessing relatively low polarity.[21] We have previously reported efficient CMA1:PVK solution-processed OLEDs, using a CMA1 concentration of 20% by weight.[4] Figure 2a presents the steady-state absorption and photoluminescence spectra of CMA1 doped in to PVK host at concentrations from 100% (neat CMA1) to 5% by weight, representing the range of dopant concentrations over which efficient OLED

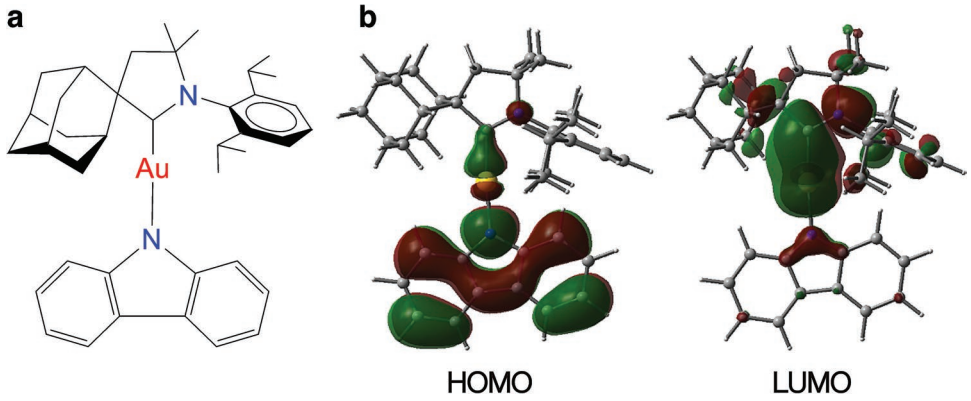

Figure 1. a) Chemical structure of CMA1. b) HOMO and LUMO wavefunctions of CMA1 from DFT calculations (MN15 functional/def2-TZVP basis set), red/green corresponds to positive/negative sign of wavefunctions.

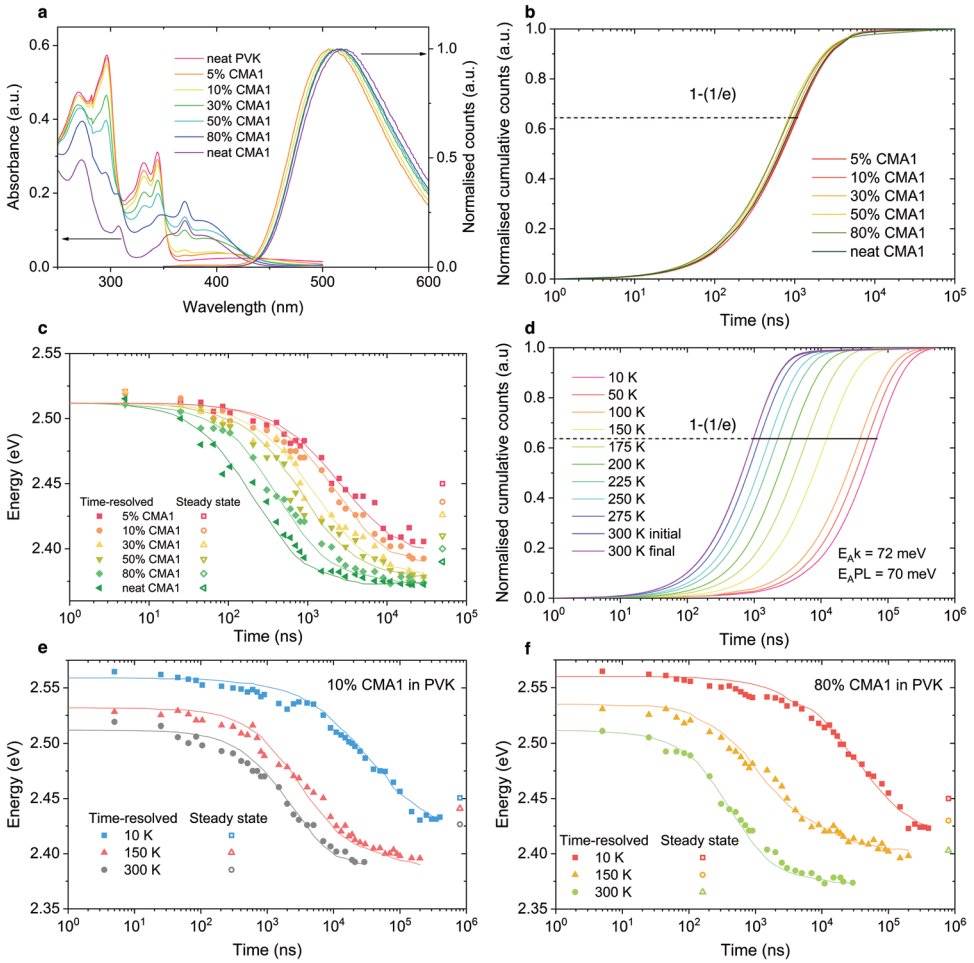

Figure 2. a) Steady-state absorption and photoluminescence of CMA1 in PVK host at different concentrations. b) Room temperature emission integral of CMA1 and PVK composites, with 1 − (1/e) labeled as the characteristic luminescence lifetime. c) Room temperature time-resolved PL peak energy of CMA1 in PVK at different concentrations to track the spectral diffusion. Lines are results of Monte-Carlo simulation. d) Cryogenic emission integral of 10% CMA1 in PVK with 1 − (1/e) labeled as the characteristic luminescence lifetime. "Initial data taken at 300 K before cooling the film to 10 K, "Final" data upon warming back to 300 K after low-temperature measurements. Two activation energies are labeled, $E_A k$ is extracted from the PL decay rate against temperature, and E_APL is extracted from the integrated PL intensity against temperature. e, f) Cryogenic time resolved PL peak position of 10% and 80% CMA1 in PVK at 10, 150, and 300 K. Lines are results of Monte-Carlo simulation.

devices have been shown to be achievable.[12] The absorption of CMA1 in PVK is dominated by parasitic host absorption and a weak scattering tail, which obscures the exact CMA1 absorption edge. PL data are more revealing; when decreasing the concentration of CMA1 in the host–guest composite from 100% to 5%, the position of the steady-state photoluminescence peak energy blueshifts by ≈60 meV, from 2.39 to 2.45 eV. Photoluminescence quantum efficiency (PLQE) of these films ranges from 67% to 94%, calculated using the De Mello method.[22] The luminescence lifetime of CMA1 in host remains relatively constant, varying from 0.97 to 1.04 µs between 100% and 5% concentration. These values are tabulated in Table S1 in the Supporting Information.

Figure 2c presents time-resolved PL peak energy over time as a function of concentration at room temperature. Spectral migration is observed over the lifetime of the excited state, with migration rate dependent on dopant concentration. The spectral relaxation shifts on a logarithmic time scale with increasing concentration. This implies that the diffusion process takes place via the dopant, and via an electronic coupling between dopants that depends exponentially on distance, such as a Dexter-type transfer.[23] At high dopant concentration, the peak position saturates to a constant value at long times. At low dopant concentration, migration is too slow for saturation to be observed before PL becomes undetectable. Migration rates for both high and low concentrations are reduced at low temperature, shown in Figure 2e, f and steady-state PL peak energies blueshift with decreasing temperature. The luminescence rate of CMA1 in PVK is strongly thermally activated above 120 K, increasing by nearly two orders of magnitude between 10 and 300 K, with characteristic activation energy of 72 meV for 10% CMA1 and 76 meV for 80% CMA1, see Figure 2d and Figure S4 in the Supporting Information. The total time-integrated luminescence increases with the same activation energy (Figure S5, Supporting Information), indicating that thermal activation is primarily of the radiative triplet decay rate. Calculations from

thermally activated decay rates are shown in Equations S1 and S2 in the Supporting Information. The observed temperature dependence is consistent with the diffusion of triplet excitons, for example as reported in neat films of poly(p-phenylene) type conjugated polymers.[24]

We model this behavior by considering that spectral migration occurs via triplet diffusion through a disordered density of emitter states, as described by Movaghar et al.[25] By applying a Monte-Carlo simulation of 3D triplet diffusion, we find that a Dexter-type dependency of hopping probability on intermolecular distance reproduces the observed concentration-dependent migration rate, with the long-time saturation of peak position occurring where triplets are able to relax to the tail of their density of states (DOS). We find that a fixed density of states for all concentrations is sufficient to model the trend observed. Moreover, we find that a Marcus-type activated hopping probability (Equation S3, Supporting Information) is required to reproduce the observed temperature dependence.[26] By fitting the experimental data, we extract a characteristic reorganization energy λ of 240 meV, corresponding to an activation energy of $E_a = \lambda/4 = 60$ meV. We note that the trend observed cannot be reproduced using a Miller–Abrahams-type hopping probability, which does not account for reorganization.[24] Emission is in general from a non-equilibrium ensemble of triplet excited states, with restriction of triplet diffusion able to tune emission energy over a small (60 meV) range. Only at high dopant concentration and higher temperatures are photoexcited triplets able to relax to a quasi-equilibrium energy in the tail of the density of states within their emission lifetime.[27] Note that the steady-state emission energy reflects the weighted time-integrated signal so that it contains contributions from across the DOS. At quasi-equilibrium in solid films, PL peak energies are within ≈10 meV of those observed in low polarity solvents (benzene and toluene), which we take as evidence that the tail of the density of states represents molecules close to the fully relaxed S_1 geometry. The blueshift in steady-state PL at decreased temperature results from the reduction in diffusion rate outcompeting the decrease in emission rate.

To explore the generality of this effect, **Figure 3** presents the dependence of steady-state luminescence peak energy on CMA1 concentration for a range of polymer and small molecule host materials with high triplet energies, deposited as thin films from solution. For all hosts lacking a significant permanent electric dipole, calculated by DFT (B3LYP/6-31G**), a universal blueshift is observed as concentration decreases, very close in magnitude to that observed in PVK. We interpret this as evidence that triplet diffusion between guest emitters is primarily limited by emitter spacing, and relatively insensitive to the nature of the intervening host. We likewise infer that molecular relaxation on the time scales of triplet emission plays only a minor role.

By contrast, we observe an additional shift in host molecules exhibiting permanent electric dipole moments, specifically Bis(N-carbazolyl)benzene (mCP) with 1.4 D; Bis[3,5-di(9H-carbazol-9-yl)phenyl]diphenylsilane (SimCP2) with 2.37 D; 9-(3-(9H-Carbazol-9-yl)phenyl)-3-(diphenylphosphoryl)-9H-carbazole (mCPPO1) with 3.91 D; and Diphenyl-4-triphenylsilylphenyl-phosphine oxide (TSPO1) with 4.1 D.

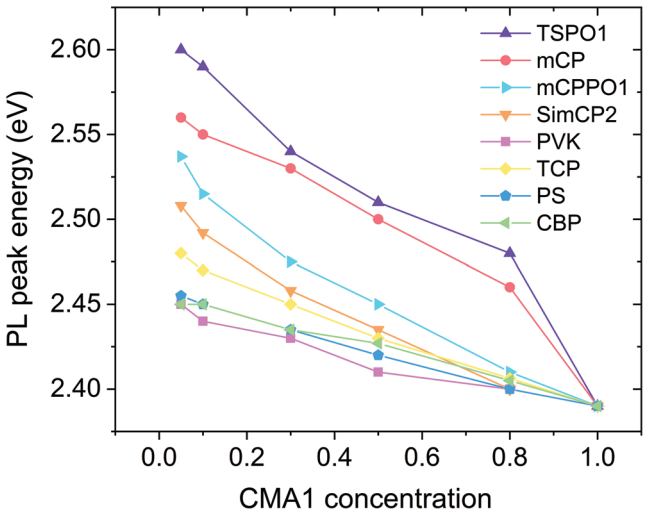

Figure 3. Steady-state PL peak energy of CMA1 in a range of hosts varying weight concentrations from 100% to 5%.

Chemical structures, electric dipole moments and steady-state photoluminescence spectra of these hosts are shown in Figures S6 and S7 in the Supporting Information. PS is polystyrene. Steady-state luminescence energy increases markedly compared to non-polar host matrices for mCP and TSPO1, with the trend of PL in mCP host consistent with that observed in electroluminescence by Conaghan et al.[12] The effect for larger host molecules SimCP2 and mCPPO1 is less pronounced. To understand the origin of this phenomenon, we focus on TSPO1, which produces the largest magnitude shift in this set.

2.3. Organic Polar Molecule Hosts and Role of Electrostatic Interactions

Steady-state absorption and photoluminescence spectra of CMA1 in TSPO1 host at various concentrations are shown in **Figure 4**a. As for PVK, the absorption of CMA1 in TSPO1 is dominated by parasitic host absorption and a weak scattering tail, which renders the exact absorption edge difficult to resolve. However, photoluminescence peak position shows a large blueshift compared to non-polar hosts, from 2.39 eV for neat CMA1 films to 2.6 eV for 5:95 wt.% CMA1:TSPO1 films. PLQE of these films are around 65% to 80%. Luminescence lifetime increases slightly from 0.97 µs (neat film) to 1.4 µs (5% CMA1), see Table S2 in the Supporting Information. Low-temperature luminescence lifetime of 10% CMA1 in TSPO1 increases by approximately a factor of 50, from 1.3 µs at 300 K to 65 µs at 10 K, see Figure 4d. The same trend is seen at higher concentration, luminescence lifetime increases from 1.02 µs at 300 K to 66 µs at 10 K for 80% CMA1 in TSPO1 (Figure S8, Supporting Information). The activation energies extracted from PL decay rate of 10% and 80% CMA1 in TSPO1 host are 79 and 77 meV, which are close to the values for PVK-hosted samples. Integrated PL intensity against temperature of 10% CMA1 in TSPO1 also yields the same activation energy as extracted from PL decay rate, indicating that

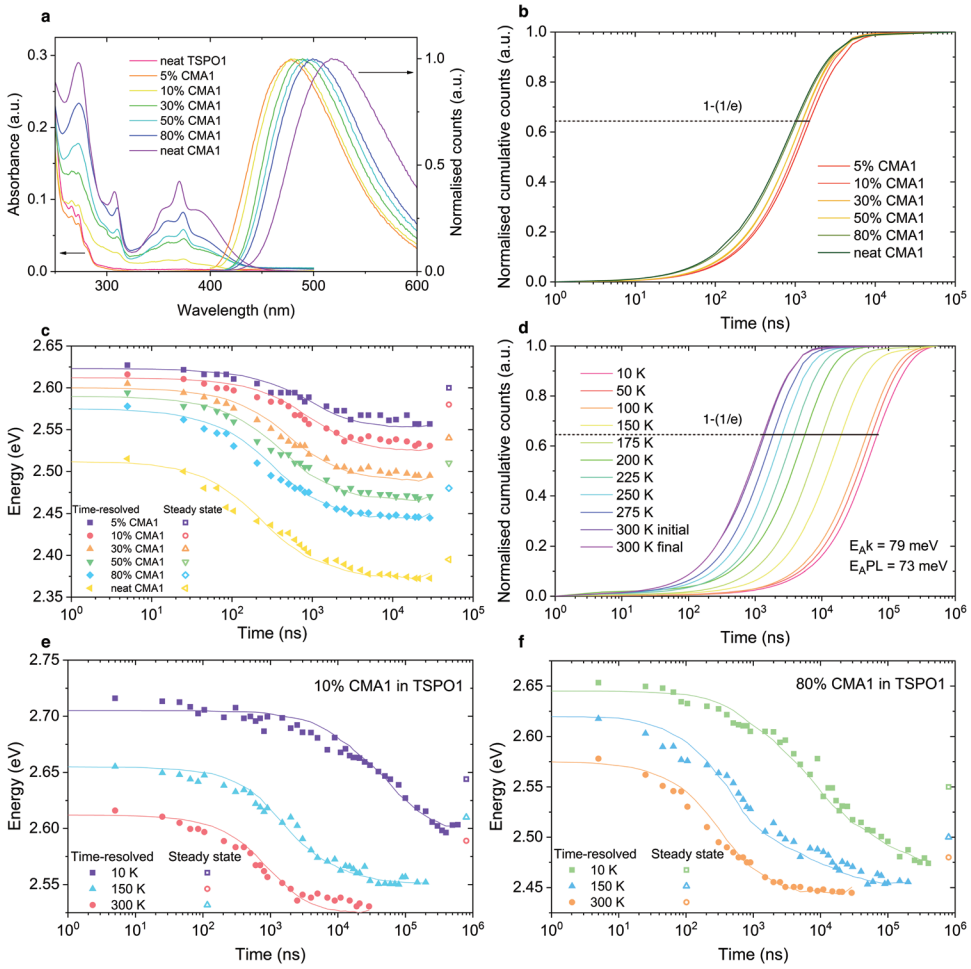

Figure 4. a) Steady-state absorption and photoluminescence of CMA1 in TSPO1 host at different concentrations. b) Room temperature emission integral of CMA1 and TSPO1 composites, with 1 − (1/e) labeled as the characteristic luminescence lifetime. c) Room temperature time-resolved PL peak energy of CMA1 in TSPO1 at different concentrations to track the spectral diffusion. Lines are results of Monte-Carlo simulation. d) Cryogenic emission integral of 10% CMA1 in TSPO1 with 1 − (1/e) labeled as the characteristic luminescence lifetime. "Initial data taken at 300 K before cooling the film to 10 K, "Final" data upon warming back to 300 K after low-temperature measurements. Two activation energies are labeled, $E_A k$ is extracted from the PL decay rate against temperature, and E_APL is extracted from the integrated PL intensity against temperature. e, f) Cryogenic time resolved PL peak position of 10% and 80% CMA1 in TSPO1 at 10, 150, and 300 K. Lines are results of Monte-Carlo simulation.

thermal activation still contributes primarily to the radiative triplet decay rate as shown in Figure S9 in the Supporting Information.

Monte-Carlo modeling of concentration- and temperature-resolved emission spectra (Figure 4c–f) reveal that this shift has two components. The first is a thermally activated spectral migration, consistent with triplet diffusion via an activated hopping process, with characteristic reorganization energy $\lambda = 240$ meV, the same as that observed for CMA1:PVK films. However, we are unable to reproduce the trend observed assuming a fixed density of states. Instead, the mean energy of the Gaussian density of states varies with concentration, shifting up by 113 meV between neat film and 5% concentration at 300 K. At the same time, the distribution narrows by 25 meV. By examining the low-temperature spectral diffusion for both high and low concentrations, see Figure 4e, f, it is clear that this effect becomes more pronounced at low temperature, shifting the PL spectra to higher energy.

X-ray diffraction and grazing-incidences wide-angle X-ray scattering measurements indicate very little evidence of crystallization of CMA1 in these TSPO1 composites (Figures S10 and S11, Supporting Information), though at low CMA1 concentration, weak host crystallization features are observed. We therefore propose that the energetic shift is due to an electrostatic interaction between the large ground state electric dipole moment of CMA1 with the smaller host dipoles, leading to orientation of the latter during deposition. Previous work by Dos Santos et al. also showed that polar matrix is able to influence molecular configuration and shifts the energy of CT states.[28] The effect is increased at low temperature, which we interpret as a reduction in thermal disorder. This solid-state solvatochromism leads to a stabilization of the ground state, and a destabilization of the excited state, as is observed in liquid solution. Unlike in solution, upon excitation the host dipoles are much less able to reorient, preserving the increased energetic splitting between the ground and excited states. As for

low-polarity hosts, this is consistent with diffusion, rather than intramolecular relaxation, dominating spectral relaxation in the solid state. Consistent with this, we find no correlation with measured glass transition temperatures (which are > 100 °C for all hosts) or with molecular weight, see Figure S12 in the Supporting Information. An additional effect is the apparent narrowing of the density of states in the MC model, which requires some explanation. We consider that this is most likely an effect of the microstructure of low-concentration TSPO1 blends. The appearance of a weak TSPO1 crystallization signal suggests an inhomogeneous local microstructure, which might reduce access to the full DOS and manifest as such a narrowing.

We thus conclude that of the 210 meV blueshift in steady-state luminescence observed between neat and dilute CMA1, ≈60 meV arises from suppressed triplet diffusion and 150 meV arises from an electrostatic host–guest interaction. In addition to providing a mechanism by which emission peak energy may be controlled over a meaningful range, solid-state solvatochromism offers a means to tune the relative energies of excited states with differing CT character, and probe the underlying mechanism of triplet harvesting.

Initial time-dependent DFT (TD-DFT) calculations of CMA1 using the PBE0 functional and def2-TZVP basis set, when referenced to experimental energies, suggested torsion leads to a crossing of the lowest singlet and triplet energies.[4] However, TD-DFT calculations using the more accurate MN15 functional, which does not suffer from the underestimation typical for TD-DFT reveal a different picture, predicting a significantly greater destabilization of S_0 by torsion, and a reduced stabilization of S_1, see Figure S13 in the Supporting Information, such that both the S_1–S_0 and T_1–S_0 energy gaps reduce as dihedral angle increases.[9] This is consistent with the combined DFT and multireference configuration interaction calculations of Föller and Marian, who find that while the S_1 state is stabilized to a greater extent than T_1 by contributions from doubly excited configurations, this is insufficient in most circumstances to invert the spin states.[14] This work also concluded that T_1 phosphorescence borrows oscillator strength from S_2, and that coupling between S_1 and T_1 is spin-vibronic in nature. Subsequent work by Penfold et al. considered couplings from S_1 to the lowest three excited triplet states and two nuclear degrees of freedom: torsion around the Au—N bond and the stretching mode of the same bond with the molecule in the relaxed S_1 geometry.[13] This work concluded that indirect spin-orbit coupling (SOC) (i.e., S_1–T_n–T_1) mediated by torsional motion may influence the rate of triplet harvesting. Taffet et al. in examining the structurally related Cu(I) analogue CMA2 concluded that intersystem crossing (ISC) was likely most effective in a sterically constrained coplanar configuration, relying on a breaking of planar symmetry by distortion of the C—Cu—N central axis to allow coupling between S_1 and T_1.[15] The underlying process coupling the T_1 state to the singlet manifold is therefore unclear. We use the experimental results above to provide new insight to this question. While CT excited states show significant negative absorption solvatochromism, excited states localized to the donor and acceptor ligands ("LE" states) are insensitive to environmental polarizability, see Figures S2 and S3 in the Supporting Information. Upon dilution in TSPO1 host, the peak-to-peak energy difference between the lowest lying emissive triplet localized to the carbazole donor (2.9 eV, Figure S14, Supporting Information) and the CT triplet decreases from 510 to 300 meV. A similar analysis considering the shift in high-energy edge gives a range 190 to around 0 meV. Despite being brought substantially closer to resonance with the localized triplets, increased CT energy leads to a slight *increase* in emission lifetime, and no meaningful change in activation energy is observed (**Figure 5**). We also find that excited state lifetime depends very weakly on whether or not a given excited molecule is structurally relaxed, with lifetime in dilute solid comparable to lifetime in dilute solution, see Table S3 in the Supporting Information. ISC time measured using transient absorption (TA) spectroscopy is likewise insensitive to the increased CT energy, and is constant at around 5–6 ps, see Figure S15 in the Supporting Information.

To establish a framework for interpreting these observations, we consider a simplified version of the chromophore which has C_{2v} symmetry,[29] with reference to molecular orbital

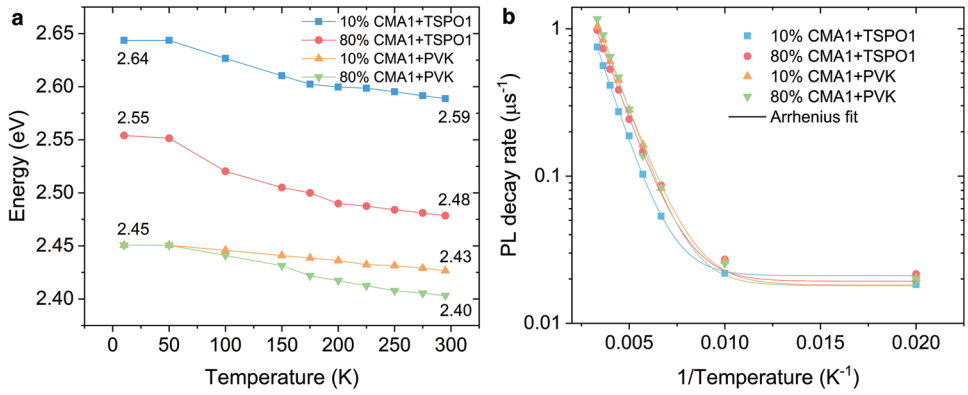

Figure 5. a) Steady-state PL peak energy of 10% and 80% concentration of CMA1 in TSPO1 and PVK host at different temperatures. PL blueshifts when decreasing the temperature. b) PL decay rate of 10% and 80% concentration of CMA1 in TSPO1 and PVK at different temperatures as a function of 1/Temperature. PL decay rate is the reciprocal of characteristic luminescence lifetime from cryogenic emission integral. The fitted curves yield activation energies: E_Ak (10% CMA1 + TSPO1) = 79 meV, E_Ak (80% CMA1 + TSPO1) = 77 meV, E_Ak (10% CMA1 + PVK) = 72 meV, E_Ak (80% CMA1 + PVK) = 76 meV.

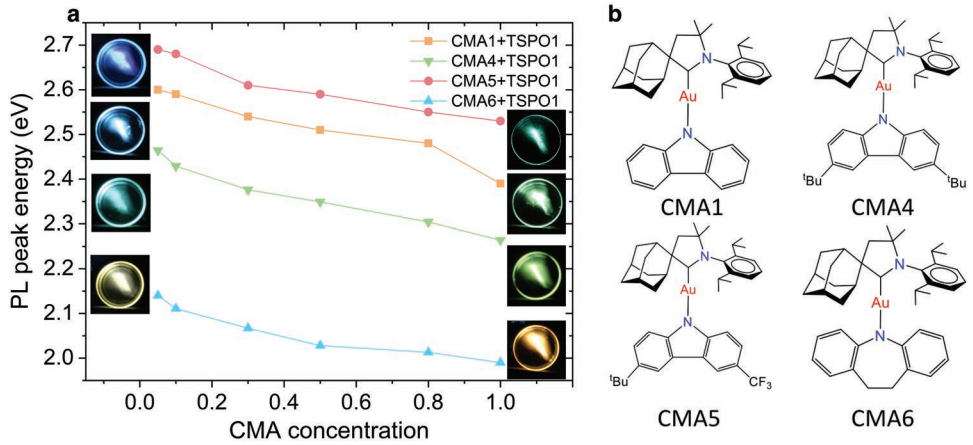

Figure 6. a) Dependence of PL peak energy of various CMAs on the doping concentration in TSPO1 host. Photographs show photoluminescence of neat CMA1, CMA4, CMA5, and CMA6 and 5% weight concentration of CMAs in TSPO1 thin films under UV illumination. b) Chemical structures of CMA1, CMA4, CMA5, and CMA6.

calculations summarized in Figures S16–S18 and Table S10 in the Supporting Information. From an examination of symmetry arguments, the locally excited Carbazole state (≈HOMO to LUMO+3) transforms as A_1 in the C_{2v} point group, the same irrep as the S_1 and T_1 states. In C_{2v}, the molecular rotations (and therefore the SOC operator) transform as all irreps except A_1. When the CMA chromophore is completely planar or twisted at 90° (both of which correspond to approximate C_{2v} symmetry), there can therefore be no direct SOC between S_1 and T_1, and nor can there be any indirect SOC via the Cz LE state (referred to as LE_1).

Since there can be no direct coupling (and therefore reverse intersystem crossing) in this idealized picture, further coupling has to be included in the model. One possibility is mixing via higher lying states which transform as irreps other than A_1. The ligand-centered state corresponding to ≈ HOMO-3 to LUMO (referred to as LE_2) transforms as B_2 and therefore its triplet form can mix with S_1. Similarly, the state formed by a predominantly HOMO-1 to LUMO transition is predominantly of CT character (referred to as CT_2) and transforms as B_1, thus its triplet form can interact with S_1 via SOC. In order for LE_2 and CT_2 to mix with T_1 there would need to be vibronic symmetry breaking, for LE_2 a B_2 mode and for CT_2 a B_1 mode. It is impossible to state for certain without calculation which of these interactions is stronger or more likely to contribute to SOC and therefore delayed fluorescence. However, the insensitivity of the photophysics to the energy of the CT states relative to the LE states suggests that the interaction could be via CT_2, which will be perturbed by electrostatic environment similarly to S_1. In addition, upon descending from C_{2v} (the symmetry of the model chromophore) to C_s (the symmetry of the actual chromophore) B_1 descends to A′; as does A_1, whereas A_2 and B_2 descend to A″. This suggests that in the reduced symmetry of the true chromophore then CT_2 may be more able to couple with T_1 than LE_2. While these arguments consider interactions via the triplet forms of LE_2 and CT_2, similar arguments also hold for interactions via the singlet forms, though this is in reality less likely due to larger energy separation. An alternative mechanism for coupling to occur between states of CT character could be vibronically allowed SOC, particularly since calculation suggests emission may result from a configuration involving twisting around the CMA bond.[30] In a partially twisted geometry (between 0° and 90°) the idealized chromophore descends in symmetry to C_2 (and the full chromophore to C_1), and S_1 and T_1 descend from A_1 to A. In this lower symmetry R_z also transforms as A, meaning that in the twisted geometry there could be direct SOC between S_1 and T_1, facilitating emission. This would also be consistent with the relative insensitivity of emission rate to host polarizability, since the S_1–T_1 energy gap is likely to be similar in range of host environments. We find little experimental evidence for beneficial coupling to LE states within energy range explored, which agrees with the "interference" effect predicted by Penfold et al.[13] This picture contrasts with several models for organic donor–acceptor emitters, where direct S_1–T_1 coupling is assumed to be very weak and emission requires spin–vibronic coupling to LE triplets.[31,32]

2.4. Extension to Other CMAs

This strategy for emission tuning and photophysical exploration does not rely on a particular emitter choice, the same approach can be extended to tune the emission of other CT emitters with a large ground-state dipole moment. In particular, we apply the same approach to emitters from the CMA family across the visible spectrum. **Figure 6**a presents thin-film photoluminescence peak energies for CMA1 and structurally related gold-bridged analogues: (CAAC)Au(3,6-di-tBucarbazole) (CMA4), (CAAC)Au(6-(tert-butyl)-3-(trifluoromethyl)-9H-carbazole) (CMA5), (CAAC)Au(10,11-dihydrodibenz[b,f]azepin-5-ide) (CMA6) embedded in the TSPO1 host. We observe a universal blue shift of PL peak energies as concentration is reduced, with similar magnitude to that of CMA1, around 200 meV.

3. Conclusion

In summary, we have demonstrated a physical approach to modulate the CT triplet energy in a donor–bridge–acceptor type organometallic emitter CMA1. The CT energy can be tuned by

around 200 meV via thermally activated diffusion and electrostatic interactions with host molecules. This shift leads to no meaningful change in ISC rate, slightly increased luminescence lifetime, and no significant change in thermal activation energy. The energy relaxation process was studied by Monte-Carlo simulations, which show that triplet diffusion can account for the experimental trends if modeled as a Marcus-type rate equation and the mean energy and width of the density of states responds to the variations of host–guest electrostatic interactions. We infer that structural relaxation is hindered in the solid state as we see little evidence for large-amplitude structural relaxation or host reorganization occurring during the excited state lifetime. Tuning of CT energy provides an experimental approach to probe the triplet harvesting mechanism and the coupling between the T_1 and S_1 states. We find that for CMA1 there is likely to be no direct spin–orbit coupling between CT states (S_1 and T_1) and ligand-centered excited states localized to the carbazole, as they transform as the same irrep. However, higher lying CT states (for example LUMO-1 to HOMO) can interact with S_1 and T_1. From the insensitivity of CMA1 photophysics to CT energy, we suggest that CT–CT coupling contributes more significantly than CT–LE coupling, offering a design rule for the realization of rapid triplet emission. We go on to show that solid-state solvatochromism may be applied to a range of gold-bridged CMAs, achieving a universal blueshift around 200 meV. Such an approach should be directly transferrable to other CT emitters with large permanent dipole moment, allowing host–guest interactions as a tool to tune electroluminescence in OLED devices over a significant range.

4. Experimental Section

General Considerations: Unless stated otherwise, all reactions were carried out in air. Solvents were distilled and dried as required. Sodium *tert*-butoxide, 3-(*tert*-butyl)phenylboronic acid, were purchased from FluoroChem, SPhos Pd G2 was purchased from Sigma–Aldrich and used as received. The carbene ligand (^{Ad}L),[33–35] *N*-(2-chloro-4-(trifluoromethyl)phenyl)acetamide and 6-(*tert*-butyl)-3-(trifluoromethyl)-9H-carbazole carbazole,[36] and complex (^{Ad}L)AuCl[8] were obtained according to literature procedures. ^{1}H and ^{13}C{^{1}H} NMR spectra were recorded using a Bruker Avance DPX-300 MHz NMR spectrometer. ^{1}H NMR spectra (300.13 MHz) and ^{13}C{^{1}H} (75.47 MHz) were referenced to CD_2Cl_2 at δ 5.32 (^{13}C, δ 53.84), C_6D_6 at δ 7.16 (^{13}C, δ 128.4), $CDCl_3$ at δ 7.26 (δ ^{13}C 77.16) ppm. Elemental analyses were performed by London Metropolitan University.

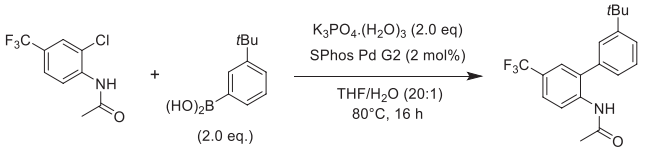

92% (1.55 g)

Synthesis of N-(3′-(tert-butyl)-5-(trifluoromethyl)-[1,1′-biphenyl]-2-yl) acetamide: *N*-(2-chloro-4-(trifluoromethyl)phenyl)acetamide (1 eq., 5.05 mmol, 1.20 g), 3-(*tert*-butyl)phenylboronic acid (2.0 eq., 10.1 mmol, 1.80 g,) and potassium phosphate trihydrate (2.0 eq., 10.1 mmol, 2.33 g) were mixed in THF/H_2O 20:1 (10 mL) and purged with argon. SPhos Pd G2 (1 mol%, 0.051 mmol, 37 mg) was added and the mixture was heated at 80 °C for 16 h. Reaction was cooled to r.t., Et_2O (30 mL) was added and the mixture was filtered through Celite. The filtrate was diluted with AcOEt (100 mL), washed with water and brine, and dried with $MgSO_4$. The solvent was evaporated and the residue was purified by silica column chromatography (PE/AcOEt) to afford the product as an off-white solid (92%, 1.55 g).

^{1}H NMR (300 MHz, $CDCl_3$): δ 8.53 (d, J = 8.7 Hz, 1H), 7.61 (pseudo dd, J = 8.7, 2.2 Hz, 1H), 7.52–7.42 (m, 3 × 1H overlapped), 7.40–7.37 (m, 1H), 7.37–7.32 (bs, NH), 7.19 (pseudo dt, J = 6.6, 1.9 Hz, 1H), 2.05 (s, 3H, Ac), 1.37 (s, 9H, *t*Bu). ^{13}C NMR (75 MHz, $CDCl_3$) δ 168.4 (s, C=O), 152.7 (s, C—*t*Bu), 138.0 (s, C_q), 136.4 (s, C_q), 132.2 (s, C_q)), 129.5 (s, CH), 127.1 (q, J = 3.6 Hz, CH—C—CF_3), 126.4 (s, CH), 126.3 (s, CH), 125.8 (s, CH), 125.5 (q, J = 3.7 Hz, CH—C—CF_3), 124.2 (q, J = 271.8 Hz, CF_3), 120.8 (s, CH), 35.1 (s, C(CH_3)$_3$), 31.5 (s, C(CH_3)$_3$), 25.0 (s, CH_3 Ac), (C_{ipso}—CF_3 was not observed due to overlap with aromatic signals). ^{19}F NMR (282 MHz, $CDCl_3$) δ -62.1 ppm. Anal. calcd. for $C_{19}H_{20}F_3NO$ 335.37): C, 68.05; H, 6.01; N, 4.18. Found: C, 68.17; H, 6.18; N, 4.31.

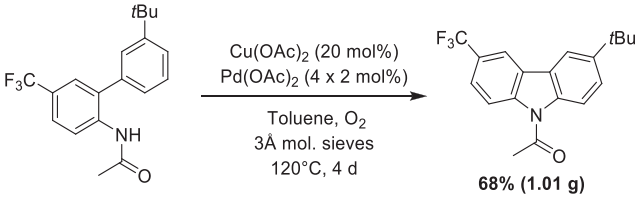

68% (1.01 g)

Synthesis of 6-(tert-butyl)-3-(trifluoromethyl)-9-acetylcarbazole: In an oven-dried Schlenk tube, under argon, *N*-(3′-(*tert*-butyl)-5-(trifluoromethyl)-[1,1′-biphenyl]-2-yl)acetamide (1 eq., 4.47 mmol, 1.50 g), $Cu(OAc)_2$ (20 mol%, 0.89 mmol, 162 mg), $Pd(OAc)_2$ (2 mol%, 0.089 mmol, 20 mg), and 3 Å molecular sieves were mixed in toluene (20 mL). The flask was purged by oxygen and heated at 120 °C. Reaction completion was followed and a portion of $Pd(OAc)_2$ was added each day (3 × 2 mol%, 3 × 20 mg). After 2 d, reaction was completed. The mixture was cooled to r.t., diluted with AcOEt (60 mL) and filtered through Celite. The filtrate was diluted with AcOEt (100 mL) washed with water and brine and dried with $MgSO_4$. The solvent was evaporated and the residue was purified by silica column chromatography (PE/AcOEt) to afford the product as an off-white solid (68%, 1.01 g).

^{1}H NMR (300 MHz, $CDCl_3$): δ 8.46 (d, J = 8.8 Hz, 1H, CH^1), 8.27 (pseudo s, 1H, CH^4), 8.04 (d, J = 2.1 Hz, 1H, CH^5), 8.01 (d, J = 8.9 Hz, 1H, CH^8), 7.71 (pseudo dd, J = 8.8, 1.9 Hz, 1H, CH^2), 7.60 (dd, J = 8.9, 2.1 Hz, 1H, CH^7), 2.90 (s, 3H, Ac), 1.45 (s, 9H, *t*Bu). ^{13}C NMR (75 MHz, $CDCl_3$) δ 170.1 (s, C=O), 147.5 (C—*t*Bu), 140.9 (s, C_q), 137.1 (s, C_q), 126.8 (s, C_q), 126.1 (s, CH^7), 126.0 (q, J = 32.6 Hz, C—CF_3), 125.6 (s, C_q), 124.7 (q, J = 271.7 Hz, CF_3), 124.2 (q, J = 3.6 Hz, CH^2), 117.0 (s, CH^1 overlapped with CH^4), 116.9 (q, J = 3.9 Hz, CH^4 overlapped with CH^1), 116.8 (s, CH^5), 115.6 (s, CH^8), 34.9 (s, C(CH_3)$_3$, 31.8 (C(CH_3)$_3$, 27.8 (s, CH_3 Ac). ^{19}F NMR (282 MHz, $CDCl_3$) δ -61.2. Anal. calcd. for $C_{19}H_{18}F_3NO$ (333.35): C, 68.46; H, 5.44; N, 4.20. Found: C, 68.13; H, 5.68; N, 3.97.

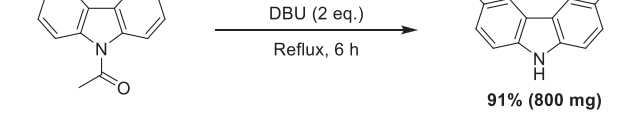

91% (800 mg)

Synthesis of 6-(tert-butyl)-3-(trifluoromethyl)-9H-carbazole: DBU (2 eq., 6.06 mmol, 904 µL) was added to 6-(*tert*-butyl)-3-(trifluoromethyl)-9-acetylcarbazole (1 eq., 3.03 mmol, 1.01 g) in MeOH (30 mL), and the mixture was refluxed for 6 h. The reaction was cooled to r.t. and volatiles were evaporated. AcOEt (120 mL) was added, washed with water and brine, and dried over $MgSO_4$. The residue was purified by silica column chromatography (PE/AcOEt) to afford the product as a white solid (91%, 800 mg).

^{1}H NMR (300 MHz, $CDCl_3$): δ 8.37 (s, 1H, CH^4), 8.16 (bs, 1H, NH), 8.12 (pseudo s, 1H, CH^5), 7.64 (pseudo dd, J = 8.5, 1.7 Hz, 1H, CH^2), 7.56 (dd, J = 8.6, 1.9 Hz, 1H, CH^8), 7.47 (d, J = 8.5 Hz, 1H, CH^1), 7.41 (d, J = 8.6 Hz, 1H, CH^7), 1.45 (s, 9H, *t*Bu). ^{13}C NMR (75 MHz, $CDCl_3$) δ

143.6 (s, C—*t*Bu), 141.5 (s, C_q), 138.2 (s, C_q), 125.5 (q, J = 271.2 Hz, CF_3), 125.0 (s, CH^7), 123.4 (s, C_q), 122.8 (s, C_q), 122.5 (q, J = 3.7 Hz, CH^2), 121.7 (q, J = 32.1 Hz, C–CF_3), 117.9 (q, J = 4.1 Hz, CH^4), 116.8 (s, CH^5), 110.7 (s, CH^1), 110.6 (s, CH^8), 34.9 (s, $C(CH_3)_3$), 32.1 (s, $C(CH_3)_3$). ^{19}F NMR (282 MHz, $CDCl_3$) δ -60.1. Anal. calcd. for $C_{17}H_{16}F_3N$ (291.32): C, 70.09; H, 5.54; N, 4.81. Found: C, 69.82; H, 5.72; N, 4.63.

Synthesis of (^{Ad}CAAC)Au(6-(tert-butyl)-3-(trifluoromethyl)-9H-carbazole) (CMA5): In a Schlenk tube, (^{Ad}L)AuCl (3.52 g, 5.77 mmol,), 6-(*tert*-butyl)-3-(trifluoromethyl)-9H-carbazole (1.68 g, 5.77 mmol), and tBuONa (0.56 g, 5.83 mmol,) were stirred in THF (75 mL) for 6 h. The mixture was filtered through Celite. The filtrate was concentrated and washed with hexane to afford the product as a white solid. Yield: 93% (4.65 g, 5.37 mmol).

^1H NMR (300 MHz, CD_2Cl_2): δ 8.20 (s, 1H, CH^4 Cz), 7.99 (d, J = 2.0 Hz, 1H CH^5 Cz), 7.71 (t, J = 7.8 Hz, 1H, *p*-CH Dipp), 7.47 (d, J = 7.8 Hz, 2H, *m*-CH Dipp), 7.30 (dd, J = 8.6, 2.0 Hz, 1H, CH^7 Cz), 7.25 (dd, J = 8.6, 1.5 Hz 1H, CH^2 Cz), 6.87 (d, J = 8.6 Hz, 1H, CH^8 Cz), 6.42 (d, J = 8.6 Hz, 1H, CH^1 Cz), 4.31 (d, J = 12.9 Hz, 2H, CH_2 Adamantyl), 2.90 (Sept, J = 6.7 Hz, 2H, CH *i*Pr Dipp), 2.45 (pseudo s, 2H + 1H, CH_2 CAAC overlapping with CH Adamantyl), 2.19—1.86 (m, 11H, Adamantyl), 1.44 (s, 6H, $C(CH_3)_2$ CAAC), 1.39 (s, 9H, *t*Bu), 1.36—1.30 (m, 12H, CH_3 *i*Pr Dipp). ^{13}C NMR (75 MHz, CD_2Cl_2) δ 244.1 (s, C: CAAC), 151.9 (s, C_q Cz), 148.8 (s, C_q Cz), 146.2 (s, *o*-C Dipp), 140.4 (s, C—*t*Bu), 136.7 (s, *i*-C Dipp), 130.0 (s, *p*-CH Dipp), 26.8 (q, J = 270.3 Hz, CF_3), 123.9 (s, C_q Cz), 123.8 (s, C_q Cz), 123.0 (s, CH^7 Cz), 119.8 (q, J = 3.2 Hz, CH^2 Cz), 117.1 (q, J = 31.3 Hz, C—CF_3 overlapping with CH^4 Cz), 116.9 (q, J = 4.2 Hz, CH^4 Cz overlapping with C–CF_3), 115.9 (s, CH^5 Cz), 114.0 (s, CH^1 Cz), 113.9 (s, CH^8 Cz), 77.6 (s, s, $C(CH_3)_2$ CAAC), 64.5 (s, C—C: CAAC), 49.1 (s, CH_2 CAAC), 39.4 (s, Adamantyl), 37.6 (s, Adamantyl), 35.8 (s, Adamantyl), 34.8 (s, 2 C overlapped, $C(CH_3)_3$ and CH Adamantyl) 32.2 (s, $C(CH_3)_3$) 29.6 m, 2 C overlapped, $C(CH_3)_2$ and CH *i*Pr Dipp), 28.6 (s, Adamantyl), 27.7 (s, Adamantyl), 26.5 (s, CH_3 *i*Pr Dipp), 23.4 (s, CH_3 *i*Pr Dipp). ^{19}F NMR (282 MHz, CD_2Cl_2) δ -59.1. Anal. calcd. for $C_{44}H_{54}AuF_3N_2$ (864.89): C, 61.10; H, 6.29; N, 3.24. Found: C, 61.35; H, 6.07; N, 3.43.

Synthesis of (^{Ad}CAAC)Au(10,11-dihydrodibenz[b,f]azepin-5-ide) (CMA6): Following the procedure described for CMA5, the complex was made from (^{Ad}CAAC)AuCl (0.2 g, 0.33 mmol), NaO^{t}Bu (33 mg, 0.33 mmol) and 10,11-dihydro-5H-dibenz[b,f]azepine (64.3 mg, 0.33 mmol) as an orange powder. Yield: 0.169 g (0.22 mmol, 66%).

^1H NMR (300 MHz, CD_2Cl_2): δ 7.53 (t, J = 7.6 Hz, 1H, aryl), 7.30 (d, J = 7.6 Hz, 2H, aryl), 6.75 (d, J = 7.4 Hz, 2H, azepine CH^4), 6.69 (d, J = 7.4 Hz, 2H, azepine CH^1), 6.62 (t, J = 7.4 Hz, 2H, azepine CH^3), 6.43 (t, J = 7.4 Hz, 2H, azepine CH^2), 3.95 (d, J = 13.2 Hz, 2H, CH_2), 2.89 (s, 4H, CH_2 azepine), 2.83 (sept, J = 6.6 Hz, 2H, C*H*Me_2), 2.14—1.69 (m, 14H, adamantyl CH and CH_2), 1.36 (s, 6H, $C(CH_3)$), 1.34 (d, J = 6.6 Hz, 6H, CHMe_2), 1.30 (d, J = 6.6 Hz, 6H, CHMe_2). ^{13}C NMR (75 MHz, CD_2Cl_2) δ 242.3 (C carbene), 153.9 (*ipso*-CN azepine), 145.4 (*o*-C), 136.4 (*ipso*-C), 129.8 (*p*-CH), 129.5 (azepine CH^4), 127.0 (azepine *ipso*-C), 125.7 (azepine CH^3), 125.4 (*m*-CH), 124.5 (azepine CH^1), 116.7 (azepine CH^2), 76.6 (C_q), 64.1 (C_q), 48.8 (CH_2), 39.3 (CH_2), 37.2 (CH), 36.4 (CH_2), 35.0 (CH_2), 34.8 (azepine CH_2), 29.3, 28.0, 27.6, 26.0, 23.4 (CH_3). Anal. calcd. for $C_{41}H_{51}N_2Au$ (768.82): C, 64.05; H, 6.69; N, 3.64. Found: C, 64.27; H, 6.83; N, 3.51.

Synthesis of *(^{Ad}CAAC)Au(Carbazole) (CMA1)* and *(^{Ad}CAAC)Au(3,6-di-tBucarbazole) (CMA4)* can be referred to the previous paper by Di et al.[4]

Sample Preparation: Host–guest thin films of different weight ratios were made from chlorobenzene solution in 20 mg mL^{-1} concentration. These well-mixed solutions were spun inside a nitrogen filled glove box onto pre-cleaned fused quartz (Spectrosil) substrates at 1200 r.p.m. for 40 s at room temperature to form thin films. Samples were stored in nitrogen glovebox to minimize degradation. Solution samples of various solvents were prepared as 1 mg mL^{-1} in the nitrogen glovebox, deoxygenated and sealed in 1 mm path length QS grade quartz cuvettes.

UV–vis–NIR Spectrophotometer: Shimadzu UV-3600 Plus spectrophotometer was used to measure the steady-state absorbance of samples, which comprises three detectors: a PMT (photomultiplier tube) for the ultraviolet and visible regions and InGaAs and cooled PbS detectors for the near-infrared region. The detectable wavelength range is between 185 and 3300 nm with resolution of 0.1 nm.

Photoluminescence Spectrometer: The FLS980 spectrofluorimeter was used to measure steady-state luminescence spectra. An R928P PMT detector was used in this experiment, with a wavelength range of 200–870 nm and a dark count rate of <50 cps (at –20 °C). The detector is operated in single photon counting mode. The PL spectra of CMA1 were collected from 350 to 650 nm with a resolution of 1 nm. Samples were excited by a 450 W Xe1 xenon arc lamp. The light from the xenon arc is focused into the monochromators by using an off-axis ellipsoidal mirror.

Room Temperature and Cryogenic ns–µs Time-Resolved Photoluminescence Measurements: Time-resolved photoluminescence spectra were measured by an electrically gated intensified CCD (ICCD) camera (Andor iStar DH740 CCI-010) connected to a calibrated grating spectrometer (Andor SR303i). Samples were photoexcited by 400 nm femtosecond laser pulses which were created by second harmonic generation in a ß-barium borate crystal from the fundamental (wavelength = 800 nm, pulse width = 80 fs) of a Ti: Sapphire laser system (Spectra-Physics Solstice), at a repetition rate of 1 kHz. A 425-nm long-pass filter was used to prevent scattered laser signal from entering the camera. Temporal evolution of the PL emission was recorded by stepping the ICCD gate delay with respect to the trigger pulse. The minimum gate width of the ICCD was 5 ns. Cryogenic measurements were carried out using an Oxford Instruments Optistat Dynamic continuous flow cryostat with liquid helium coolant, and an ITC 502 S temperature control unit.

The 1 kHz repetition rate of the laser used in this experiment restricts the maximum accurate measurable of lifetimes to 1 ms. For non-exponential luminescence decays in the solid state, a characteristic lifetime rather than monoexponential decay time is quoted. The time taken for the delayed component was chosen to reach 63% ($1 - (1/e)$) of the total emission integrated from 0 to 550 µs. This allows direct comparison to lifetimes extracted from monoexponential decays recoded in, e.g., solution phase.

Monte-Carlo Simulations: A cubic lattice with 101 × 101 × 101 triplet sites, where site energies were drawn randomly from a Gaussian distribution, was employed for the Monte-Carlo simulation. The initial triplet excitation was placed in the center of the lattice. The hopping rates to the nearest 125 neighbors were calculated using Equation S3 in the Supporting Information. The hopping probability to each site and the overall hopping time were computed with Equations S4 and S5 in the Supporting Information. The triplet excitation was allowed to jump to one of the 125 sites randomly according to the hopping probabilities and the hopping time was added to the total simulation time. The procedures above were repeated until a pre-defined diffusion time was reached. The parameterization for Figures 2 and 4 is described in detail in the Supporting Information.

Transient Absorption Spectroscopy: Films were drop-cast from solution, 60 µL per film on 13 mm quartz discs heated to 70 °C. Solutions of CMA1 and TSPO1 in chlorobenzene were made at 20 mg mL^{-1} concentrations, overnight heated at 70 °C to dissolve the TSPO1 and mixed in the appropriate ratio to achieve the desired host-guest concentration (5 wt.%). Films were made and kept in a glovebox and encapsulated using a glass slide and epoxy prior to being measured. Drop-cast films had an optical density of 0.12 at 400 nm (the pump wavelength). The main laser used was a Spectra Physics Solstice Ti:Sapphire laser, pulse width 80 fs and repetition rate of 1 kHz at 800 nm. The pump beam was frequency-doubled using a BBO to give 400 nm pulses. Excitation fluence was varied from 9 to 60 µJ cm^{-2}. The probe beam was generated from the 800 nm fundamental using a non-collinear optical parametric amplifier, built in-house. The probe was further split into a probe and reference, with only the probe beam overlapping with the pump on the sample. The pump-probe delay was controlled using a computer-controlled delay stage. A Hamamatsu G11608-512 InGaAs dual-line array detector was used to measure the transmitted probe and reference.

Computational Details: DFT calculations of CMA1 were carried out by the global hybrid MN15 functional by Truhlar and coworkers[37] in combination with the def2-TZVP basis set by Ahlrichs and

coworkers.[38,39] Relativistic effective core potential of 60 electrons was used to describe the core electrons of Au.[40] The ground state was studied by DFT and the excited states by TD-DFT.[41] The employed method provides excited state energies that do not suffer from underestimation typical for TD-DFT,[42,43] as indicated by the recent work on closely related molecules[7,9] as well as by comparison to T_1 energies calculated by unrestricted DFT: the unrestricted and TD-DFT T_1 energies differed by only 0.004 eV. All calculations were carried out by Gaussian 16.[44] DFT calculations of dipole moments were carried out using the B3LYP[45] functional with the 6–31G** basis set, and were carried out in ORCA 4.1.0.[46]

Supporting Information

Supporting Information is available from the Wiley Online Library or from the author.

Acknowledgements

The authors thank Russel Holmes for fruitful discussions. The authors thank the Diamond Light Source for access to the I07 beamline and for the help during the GIWAX measurements. The authors thank Edoardo Ruggeri for helpful discussions on GIWAX data. The authors thank Dr. Emrys Evans for helpful guidance on the DFT calculations of host dipole moment. J.F. acknowledges his parents for financial support on his Ph.D. L.Y. acknowledges Trinity-Barlow Scholarship. D.C. acknowledges the support from the Royal Society (grant no. UF130278). S.T.E.J. acknowledges support from the Royal Society (grant no. RG140472). A.P.M.R. acknowledges support from the Royal Society (grant no. RGF\EA\180041) and the Osk, Huttunen fund. M.B. acknowledges the ERC Advanced Investigator Award (grant no. 338944-GOCAT). A.S.R. acknowledges support from the Royal Society (grant no. URF\R1\180288 and RGF\EA\181008). This work was supported by the EPSRC Cambridge NanoDTC, EP/L015978/1 and EP/M005143/1. T.J.H.H. acknowledges a Research Fellowship from Jesus College, Cambridge. A.K. and H.B. acknowledge financial support by the EC through the Horizon 2020 Marie Sklodowska-Curie ITN project TADF life. M.L. acknowledges the Academy of Finland Flagship Programme, Photonics Research and Innovation (PREIN), decision 320166. The computations were made possible by use of the Finnish Grid and Cloud Infrastructure resources (urn:nbn:fi:research-infras-2016072533). The data set underpinning this work can be accessed at: https://doi.org/10.17863/CAM.46273.

Conflict of Interest

The authors declare no conflict of interest.

Keywords

carbene-metal-amide, coupling mechanism, emission tuning, organometallics, thermally-activated delayed fluorescence

Received: October 22, 2019
Revised: November 15, 2019
Published online:

[1] C. W. Tang, S. A. Vanslyke, *Appl. Phys. Lett.* **1987**, *51*, 913.
[2] M. A. Baldo, D. F. O'Brien, Y. You, A. Shoustikov, S. Sibley, M. E. Thompson, S. R. Forrest, M. A. Baldo, D. F. O'Brien, Y. You, A. Shoustikov, S. Sibley, M. E. Thompson, *Nature* **1998**, *395*, 151.
[3] J. Lee, H.-F. Chen, T. Batagoda, C. Coburn, P. I. Djurovich, M. E. Thompson, S. R. Forrest, *Nat. Mater.* **2015**, *15*, 92.
[4] D. Di, A. S. Romanov, L. Yang, J. M. Richter, J. P. H. Rivett, S. Jones, T. H. Thomas, M. A. Jalebi, R. H. Friend, M. Linnolahti, M. Bochmann, D. Credgington, *Science* **2017**, *356*, 159.
[5] M. A. Baldo, C. Adachi, S. R. Forrest, *Phys. Rev. B* **2000**, *62*, 10967.
[6] S. Reineke, K. Walzer, K. Leo, *Phys. Rev. B* **2007**, *75*, 125328.
[7] A. S. Romanov, L. Yang, S. T. E. Jones, D. Di, O. J. Morley, B. H. Drummond, A. P. M. Reponen, M. Linnolahti, D. Credgington, M. Bochmann, *Chem. Mater.* **2019**, *31*, 3613.
[8] A. S. Romanov, M. Bochmann, *Organometallics* **2015**, *34*, 2439.
[9] A. S. Romanov, S. T. E. Jones, L. Yang, P. J. Conaghan, D. Di, M. Linnolahti, D. Credgington, M. Bochmann, *Adv. Opt. Mater.* **2018**, *6*, 1801347.
[10] R. Hamze, S. Shi, S. C. Kapper, D. S. M. Ravinson, L. Estergreen, M. C. Jung, A. C. Tadle, R. Haiges, P. I. Djurovich, J. L. Peltier, R. Jazzar, G. Bertrand, S. E. Bradforth, M. E. Thompson, *J. Am. Chem. Soc.* **2019**, *141*, 8616.
[11] R. Hamze, J. L. Peltier, D. Sylvinson, M. Jung, J. Cardenas, R. Haiges, M. Soleilhavoup, R. Jazzar, P. I. Djurovich, G. Bertrand, M. E. Thompson, *Science* **2019**, *363*, 601.
[12] P. J. Conaghan, S. M. Menke, A. S. Romanov, S. T. E. Jones, A. J. Pearson, E. W. Evans, M. Bochmann, N. C. Greenham, D. Credgington, *Adv. Mater.* **2018**, *30*, 1802285.
[13] S. Thompson, J. Eng, T. J. Penfold, *J. Chem. Phys.* **2018**, *149*, 014304.
[14] J. Föller, C. M. Marian, *J. Phys. Chem. Lett.8*, **2017**, 5643.
[15] E. J. Taffet, Y. Olivier, F. Lam, D. Beljonne, G. D. Scholes, *J. Phys. Chem. Lett.* **2018**, *9*, 1620.
[16] N. A. Kukhta, H. F. Higginbotham, T. Matulaitis, A. Danos, A. N. Bismillah, N. Haase, M. K. Etherington, D. S. Yufit, P. R. McGonigal, J. V. Gražulevičius, A. P. Monkman, *J. Mater. Chem. C* **2019**, *7*, 9184.
[17] T. Northey, J. Stacey, T. J. Penfold, *J. Mater. Chem. C* **2017**, *5*, 11001.
[18] T. J. Penfold, F. B. Dias, A. P. Monkman, *Chem. Commun.* **2018**, *54*, 3926.
[19] B. L. Cotts, D. G. McCarthy, R. Noriega, S. B. Penwell, M. Delor, D. D. Devore, S. Mukhopadhyay, T. S. De Vries, N. S. Ginsberg, *ACS Energy Lett.* **2017**, *2*, 1526.
[20] C. R. Hall, A. S. Romanov, M. Bochmann, S. R. Meech, *J. Phys. Chem. Lett.* **2018**, *9*, 5873.
[21] K. S. Yook, J. Y. Lee, *Adv. Mater.* **2014**, *26*, 4218.
[22] J. C. de Mello, H. F. Wittmann, R. H. Friend, *Adv. Mater.* **1997**, *9*, 230
[23] J. Lange, B. Ries, H. Bässler, *Chem. Phys.* **1988**, *128*, 47.
[24] S. T. Hoffmann, S. Athanasopoulos, D. Beljonne, H. Bässler, A. Köhler, *J. Phys. Chem. C* **2012**, *116*, 16371.
[25] B. Movaghar, M. Grünewald, B. Ries, H. Bässler, D. Würtz*Phys. Rev. B* **1986**, *33*, 5545.
[26] A. Köhler, H. Bässler, *J. Mater. Chem.* **2011**, *21*, 4003.
[27] A. Köhler, H. Bässler, *Electronic Processes in Organic Semiconductors—An Introduction*, Wiley-VCH, Weinheim, Germany **2015**.
[28] P. L. Dos Santos, J. S. Ward, A. S. Batsanov, M. R. Bryce, A. P. Monkman, *J. Phys. Chem. C* **2017**, *121*, 16462.
[29] T. J. H. Hele, D. Credgington, Theoretical description of Carbene-Metal-Amides. **2018**, arXiv:1802.00804.
[30] E. W. Evans, Y. Olivier, Y. Puttisong, W. K. Myers, T. J. H. Hele, S. M. Menke, T. H. Thomas, D. Credgington, D. Beljonne, R. H. Friend, N. C. Greenham, *J. Phys. Chem. Lett.* **2018**, *9*, 4053.
[31] M. K. Etherington, F. Franchello, J. Gibson, T. Northey, J. Santos, J. S. Ward, H. F. Higginbotham, P. Data, A. Kurowska, P. L. Dos Santos, D. R. Graves, A. S. Batsanov, F. B. DIas, M. R. Bryce, T. J. Penfold, A. P. Monkman, *Nat. Commun.* **2017**, *8*, 14987.

[32] M. K. Etherington, J. Gibson, H. F. Higginbotham, T. J. Penfold, A. P. Monkman, *Nat. Commun.* **2016**, *7*, 13680.
[33] V. Lavallo, Y. Canac, C. Präsang, B. Donnadieu, G. Bertrand, *Angew. Chem., Int. Ed.* **2005**, *44*, 5705.
[34] R. Jazzar, R. D. Dewhurst, J. B. Bourg, B. Donnadieu, Y. Canac, G. Bertrand, *Angew. Chem., Int. Ed.* **2007**, *46*, 2899.
[35] R. Jazzar, J. B. Bourg, R. D. Dewhurst, B. Donnadieu, G. Bertrand, *J. Org. Chem.* **2007**, *72*, 3492.
[36] M. Gantenbein, M. Hellstern, L. Le Pleux, M. Neuburger, M. Mayor, *Chem. Mater.* **2015**, *27*, 1772.
[37] H. S. Yu, X. He, S. L. Li, D. G. Truhlar, *Chem. Sci.* **2016**, *7*, 5032.
[38] F. Weigend, R. Ahlrichs, *Phys. Chem. Chem. Phys.* **2005**, *7*, 3297.
[39] F. Weigend, M. Häser, H. Patzelt, R. Ahlrichs, *Chem. Phys. Lett.* **1998**, *294*, 143.
[40] D. Andrae, U. Häußermann, M. Dolg, H. Stoll, H. Preuß, *Theor. Chim. Acta* **1990**, *77*, 123.
[41] F. Furche, D. Rappoport, M. Olivuccim, *Density Functional Methods for Excited States: Equilibrium Structure and Electronic Spectra in Computational Photochemistry*, Elesvier, Amsterdam, **2005**.
[42] A. Dreuw, M. Head-Gordon, *Chem. Rev.* **2005**, *105*, 4009.
[43] B. Moore, H. Sun, N. Govind, K. Kowalski, J. Autschbach, *J. Chem. Theory Comput.* **2015**, *11*, 3305.
[44] M. J. Frisch, G. W. Trucks, H. B. Schlegel, G. E. Scuseria, M. A. Robb, J. R. Chesseman, G. Scalmani, V. Barone, G. A. Petersson, H. Nakatsuji, X. Li, M. Caricato, A. Marenich, J. Bloino, B. G. Janesko, R. Gomperts, B. Mennucci, H. P. Hratchian, J. V. Ortiz, A. F. Izmaylov, J. L. Sonnenberg, D. Williams-Young, F. Ding, F. Lipparini, F. Egidi, J. Goings, B. Peng, A. Petrone, T. Henderson, D. Ranasinghe, et al. *Gaussian 16, Revision A. 03.* Gaussian. Inc. Wallingford CT **2016**.
[45] A. D. Becke, *J. Chem. Phys.* **1993**, *98*, 5648.
[46] F. Neese, *Wiley Interdiscip. Rev.: Comput. Mol. Sci.* **2012**, *2*, 73.